Quantum Fluctuations Suppress the Critical Fields in $BaCo_2(AsO_4)_2$

Shiva Safari,[1] William Bateman-Hemphill,[2] Asimpunya Mitra,[2] Félix Desrochers,[2]
Emily Z. Zhang,[2] Lubuna Shafeek,[1] Austin Ferrenti,[3, 4] Tyrel M. McQueen,[3, 4] Arkady
Shekhter,[5] Zoltán Köllö,[1] Yong Baek Kim,[2] B. J. Ramshaw,[6, 7] and K. A. Modic[1, *]

[1]Institute of Science and Technology Austria, 3400 Klosterneuburg, Austria
[2]Department of Physics, University of Toronto, Ontario M5S 1A7, Canada
[3]Institute for Quantum Matter and William H. Miller III Department of Physics and Astronomy,
Johns Hopkins University, Baltimore MD 21218, USA
[4]Department of Chemistry, The Johns Hopkins University, Baltimore, MD 21218, USA
[5]Los Alamos National Laboratory, Los Alamos New Mexico 87545, USA
[6]Laboratory of Atomic and Solid State Physics, Cornell University, Ithaca, NY, USA
[7]Canadian Institute for Advanced Research, Toronto, Ontario, Canada
(Dated: March 25, 2024)

Early efforts to realize exotic quantum ground states in frustrated magnets focused on frustration arising from the lattice geometry alone. Attention has shifted to bond-dependent anisotropic interactions, as well as further-neighbor interactions, on non-geometrically-frustrated lattices due to their greater versatility. The honeycomb magnet $BaCo_2(AsO_4)_2$ recently emerged as a candidate host for both bond-dependent (e.g. Kitaev) and third-neighbor (J_3) interactions, and has become a model experimental system due to its relatively low levels of disorder. Understanding the relative importance of different exchange interactions holds the key to achieving novel ground states, such as quantum spin liquids. Here, we use the magnetotropic susceptibility to map out the intermediate and high-field phase diagram of $BaCo_2(AsO_4)_2$ as a function of the out-of-plane magnetic field direction at $T = 1.6$ K. We show that the experimental data are qualitatively consistent with classical Monte Carlo results of the XXZ-J_1-J_3 model with small Kitaev and off-diagonal exchange couplings included. However, the calculated critical fields are systematically larger than the experimental values. Infinite-DMRG computations on the quantum model reveal that quantum corrections from a nearby ferromagnetic state are likely responsible for the suppressed critical fields. Together, our experiment and theory analyses demonstrate that, while quantum fluctuations play an important role in determining the phase diagram, most of the physics of $BaCo_2(AsO_4)_2$ can be understood in terms of the classical dynamics of long-range ordered states, leaving little room for the possibility of a quantum spin liquid.

Introduction

The spin-orbit entangled $J_{eff} = 1/2$ local moments in Co-based frustrated magnets offer novel routes to achieve exotic quantum ground states, such as a quantum spin liquid (QSL). One example is $BaCo_2(AsO_4)_2$, with a low-disorder honeycomb lattice and an ordering temperature that is suppressed well below the exchange energy scale [1]. The lattice geometry and spin-orbit coupling allow for bond-dependent interactions, such as the Kitaev interaction, and third nearest-neighbour exchange interactions, both of which lead to significant magnetic frustration. Recently explored in the context of Kitaev magnetism [2–6], $BaCo_2(AsO_4)_2$ is likely better described by the XXZ-J_1-J_3 model where the XXZ anisotropy comes from the local trigonal distortion of the oxygen octahedra [7–13]. In addition, the inclusion of small anisotropic interactions is required to explain the gap in the magnon spectrum [14]. The rich field-temperature phase diagram of $BaCo_2(AsO_4)_2$ makes it an ideal test of our ability to model frustrated spin-1/2 systems [1, 15, 16]. Furthermore, terahertz measurements recently reported the emergence of an excitation continuum with the application of a magnetic field perpendicular to the basal plane [17]. This continuum was interpreted as a signature of a field-induced QSL, and calls for a critical examination of the potential stabilization of exotic ground states in $BaCo_2(AsO_4)_2$ through the application of an out-of-plane magnetic field.

Classical Monte Carlo and molecular dynamics simulations were previously used to determine a minimal spin model by fitting neutron scattering and thermodynamic data [14]. The resulting XXZ-J_1-J_3 spin Hamiltonian provides an excellent description of the dynamical spin structure factor in zero magnetic fields and in the high-field polarized state. The classical model further captures the incommensurate ordering wave vector $|\mathbf{q}_c| = 0.27$ along the $\Gamma \rightarrow M$ direction of the zero-field ground state, and the intermediate commensurate field-induced phase with $|\mathbf{q}_c| = 1/3$ observed experimentally for an in-plane field between $B_{c1} = 0.33$ T and $B_{c2} = 0.55$ T [1, 14–16, 18]. This intermediate phase is

stabilized in the classical model by weak bond-dependent interactions [14]. Despite this success, the classical model's ability to capture the system's behaviour upon the application of a field with an out-of-plane component has yet to be tested. Indeed, if the field-induced QSL suggested in Ref. [17] is realized, significant qualitative discrepancies between the classical model and experimental observations are expected as the QSL cannot be realized in the classical model. This discourse calls for sensitive measurements of the magnetic response as a function of the external magnetic field's direction. Detailed angular information can further provide invaluable information in determining the correct values of the small anisotropic terms, which play a crucial role when a large number of states are in close energetic competition, such as in $BaCo_2(AsO_4)_2$. Moreover, these subleading interactions may be important to understand the short-range quasi-collinear (double-zig-zag-like) correlations in the incommensurate ordered state observed in spherical neutron polarimetry experiments [16]. Currently, only an incommensurate spiral and the commensurate double zig-zag state with $|\mathbf{q}_c| = 1/4$ are realized in relevant classical and quantum models, respectively [8, 14, 19].

In this work, we measure the magnetotropic susceptibility – the second derivative of the free energy with respect to magnetic field angle – of $BaCo_2(AsO_4)_2$ at $T = 1.6$ K [20, 21]. Through precise angle-dependent measurements, we map out the critical fields for both the incommensurate to commensurate transition, B_{c1}, and the commensurate to field-polarized transition, B_{c2} (Figure 1). While the Monte Carlo results of the classical XXZ-J_1-J_3 model capture the qualitative features of the field-angle phase diagram, and the ratio B_{c2}/B_{c1}, for a wide range of angles, they overestimate the overall critical field scale by a factor of roughly 1.6. Using infinite density matrix renormalization group (iDMRG) [22–26], we obtain an incommensurate ground state that is stable over a much-reduced parameter regime than predicted classically. Hence, quantum corrections to the ground state energies are likely responsible for the overestimation of the critical fields in the classical calculations.

Experiment

We use resonant torsion magnetometry [20] to measure the magnetotropic susceptibility of $BaCo_2(AsO_4)_2$ [21]. Samples were prepared as reported in Ferrenti *et al.* [27] (see SI I for additional details). Small single crystals are cut with focused-ion beam (FIB) lithography and aligned with electron back-scattered diffraction (EBSD) (see Figure 3 and the SI). These samples are welded onto a silicon micro-cantilever with FIB-deposited platinum. Measurements on FIB'ed samples were cross-checked against measurements on larger, non-FIB'ed, single crystals. Measurement on FIB'ed crystals is advantageous since their smaller size reduces the signal and thus allows us to access the entire field-angle phase diagram of a system with large magnetic anisotropy.

We measure the resonant frequency of the sample-cantilever system at its fundamental mechanical mode (Figure 3). Changing the magnetic field and field angle leads to shifts in the system's resonant frequency due to the magnetic anisotropy in the sample. These shifts are proportional to the second derivative of the free energy as a function of magnetic field angle (*i.e.* the magnetotropic susceptibility [20, 21]). In the linear response regime (*i.e.* when the magnetization grows linearly with magnetic field), the magnetotropic susceptibility is equal to $k = \mu_o(\chi_{ii} - \chi_{jj})H^2 \cos 2\theta$. Here, i and j reflect the principal axes of the magnetic susceptibility tensor that lie in the plane of vibration, and θ defines the angle between the crystallographic c-direction and the magnetic field (see Figure 1).

Results

Establishing the correspondence between the magnetization and the magnetotropic susceptibility

The distinct regions of the temperature-magnetic field phase diagram of $BaCo_2(AsO_4)_2$ have been extensively studied under an in-plane magnetic field [1, 14–17, 28] and are in agreement with our data for a largely in-plane field component in Figure 1B. $BaCo_2(AsO_4)_2$ enters an incommensurate antiferromagnetic (AFM) phase at $T_N = 5.5$ K at zero magnetic field. Under an applied magnetic field, the incommensurate phase gives way to a commensurate phase with an ↑↑↓ structure, consistent with the magnetization reaching 1/3 of the full saturated moment in the range from 0.2 T $\lesssim B \lesssim 0.5$ T (left axis of Figure 1A) [1, 14, 28]. At 1.5 K and above 0.5 T, an in-plane magnetic field polarizes the spins and saturates the magnetization at 2.5 μ_B per Co^{2+} — consistent with the calculated g-factor [1].

The step in the magnetization that marks the transition into the field-polarized phase correlates with a dip in the magnetotropic susceptibility (right axis of Figure 1A). This feature is expected because k is proportional to the anisotropic susceptibility, which itself is a field-derivative of the magnetization. We identify this feature as B_{c2}. The amplitude of the change in k at B_{c2} goes to zero along the high symmetry directions of the phase boundary (i.e. where $\partial T_N/\partial\theta \to 0$, see the inset of Figure 2B). We therefore show the magnetotropic data for $\theta = 75°$ in order to
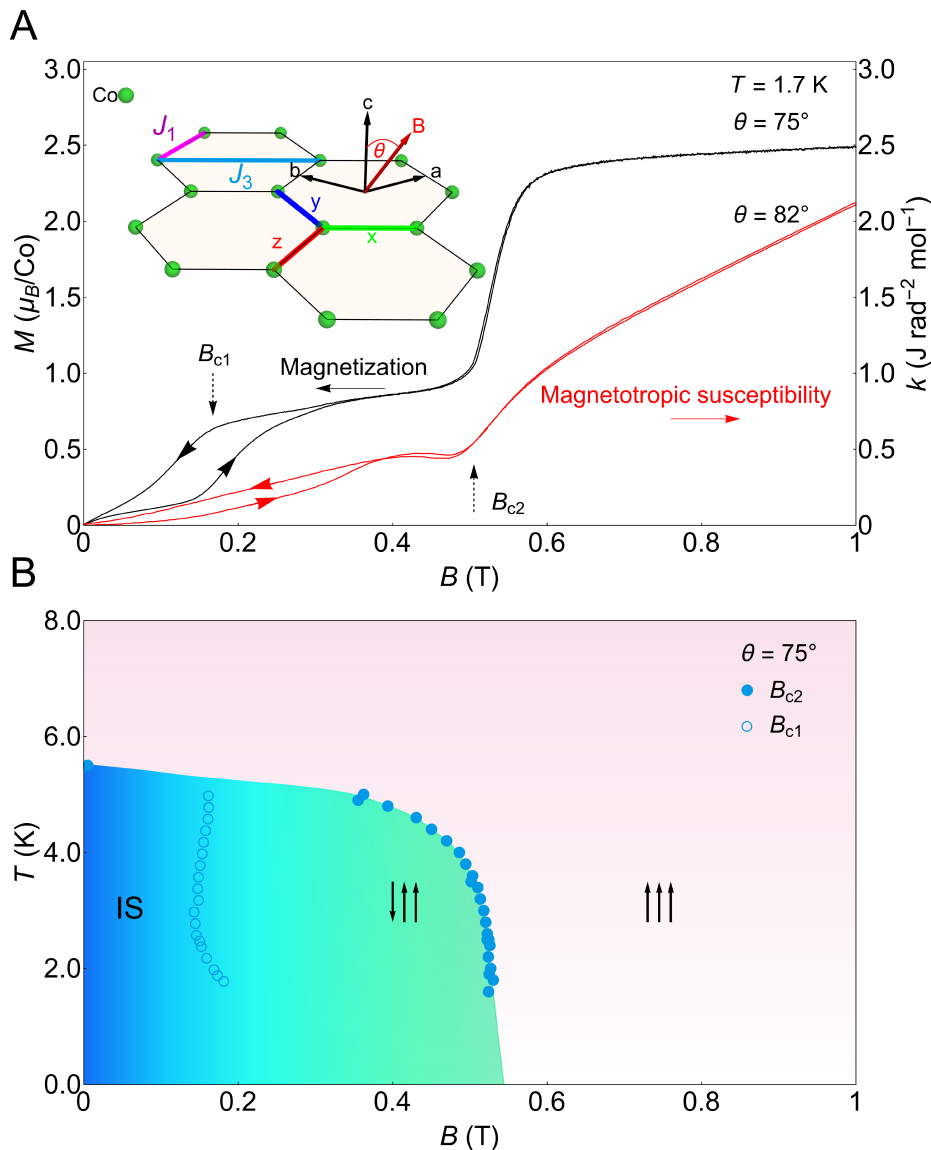
A

B

FIG. 1. **Established in-plane phase diagram of BaCo$_2$(AsO$_4$)$_2$.** A) Magnetization (left axis) and magnetotropic susceptibility (right axis) measured for a nearly in-plane magnetic field ($\theta = 75°$) to show how features correlate across different measurements techniques. Hysteresis is observed around the incommensurate to commensurate transition, B_{c1}, in both curves. The sharp increase to saturated magnetization at 0.5 T corresponds to a minimum in the magnetotropic susceptibility, with the slight mismatch in field position due to the small angular difference. The inset shows the honeycomb network of cobalt ions highlighting the first- and third-neighbor interactions, J_1 and J_3, respectively. The crystallographic axes a, b, c are shown with respect to the honeycomb bonds and θ is defined as the angle between the magnetic field direction and the c-axis. B) The temperature-magnetic field phase diagram of BaCo$_2$(AsO$_4$)$_2$ for $\theta = 75°$ constructed from magnetization and magnetotropic susceptibility data (IS = incommensurate state).

highlight B_{c2}. From field sweeps of k (black curve in Figure 2B), we also identify a region of hysteresis around a change in slope at B_{c1} that corresponds to the transition between the incommensurate and commensurate phases. B_{c1}, however, is much sharper when k is measured as a function of field angle (pink curve in Figure 2B). We therefore use the angle-sweep data to identify B_{c1} and B_{c2} in constructing the field-angle phase diagram of BaCo$_2$(AsO$_4$)$_2$.

Mapping the phase boundaries with angle

We now identify the magnetic phase transitions as the field is rotated from the in-plane direction ($\theta = 90°$) towards the c-axis ($\theta = 0°$). The magnetic easy-axes lie in the honeycomb plane. Thus, B_{c2} is pushed to higher magnetic fields
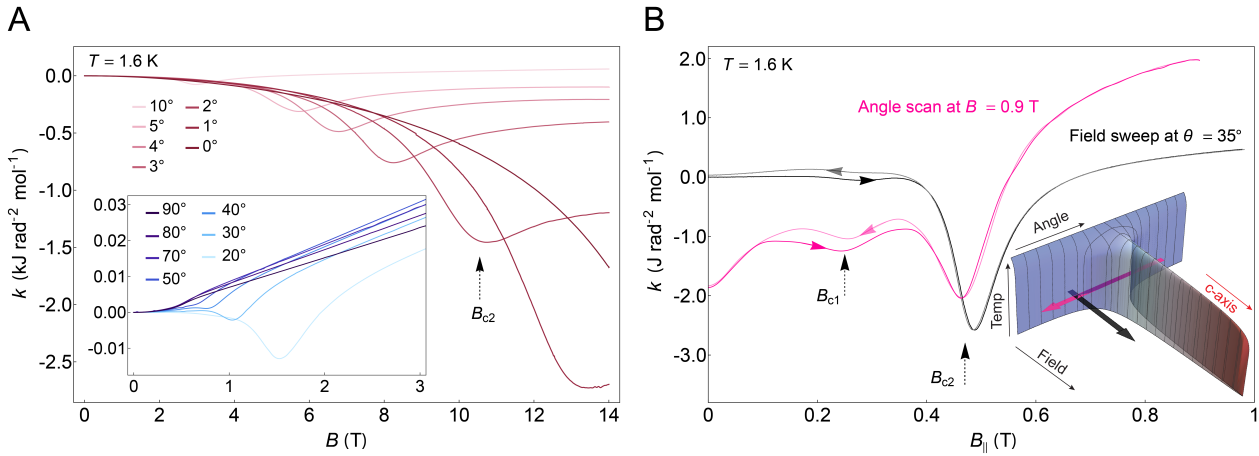
FIG. 2. **The out-of-plane magnetotropic susceptibility.** A) The magnetotropic susceptibility as a function of magnetic field applied along several directions near the c-axis. B_{c2} is highly anisotropic for magnetic fields near the c-axis. The maximum B_{c2} observed is ~ 13.5 T. Fits to the position of the minima as a function of angle are used to extract a c-axis critical field of 15 T. The inset shows similar data for field angles approaching the in-plane direction. B) The magnetotropic susceptibility measured as a function of the magnetic field at fixed angle (black curve) and as a function of angle in a fixed magnetic field (pink curve). We define the in-plane component of field as $B_{||} \equiv B \sin \theta$. B_{c1} and B_{c2} appear as minima at 0.25 T and 0.5 T, respectively, in both data sets when plotted versus $B_{||}$. The inset schematically shows how the AFM phase boundary is traversed for both measurements.

for larger out-of-plane field components (Figure 2A). Figure 2B shows two curves that cut through the schematic phase boundary as a function of both magnetic field orientation and magnetic field strength. Since the phase boundaries in $BaCo_2(AsO_4)_2$ are predominantly sensitive to the in-plane field component, we plot the data as a function of $B \sin \theta$ and find that both magnetic phase transitions scale approximately as $B_c(\theta) = B_c(90°)/|\sin \theta|$.

We find that B_{c1} is more pronounced in measurements of k as a function of magnetic field orientation, rather than field strength (Figure 2B). We therefore use angle-dependent measurements to map both critical fields across the entire phase diagram. Figure 3 shows the magnetotropic susceptibility at $T = 1.6$ K on two different samples: low-field measurements (up to 3 T) on the larger bulk crystal provide higher resolution of the intermediate field-induced phase, and the smaller FIB'ed crystal is used to track the large shift in resonant frequency through B_{c2} to higher magnetic fields (from $B = 5$ to 14 T). Both critical fields are plotted as a function of field angle in Figure 4.

Figure 3 illustrates that the critical fields are almost entirely determined by the in-plane component of the magnetic field. Only when the field is very close to the c-axis is the divergence of the critical field cut off to a finite value (Figure 4). This behavior (for both B_{c1} and B_{c2}) is captured by

$$B_c = \frac{B_c^0}{\sqrt{\sin^2 \theta + \frac{1}{\gamma^2}\cos^2 \theta}}, \tag{1}$$

where $B_c^0 \equiv B_c(\theta = 90°)$ is the in-plane critical field, and γ is the anisotropy parameter defined such that $B_c^0 \gamma$ is the out-of-plane critical field. We find $\gamma = 31$ for B_{c2}, which means that the correction to $\sin\theta$ scaling is not resolvable in the data until $\theta \lesssim 2°$ (Figure 11). This is significantly more anisotropic than RuCl$_3$, where γ is less than 10 [29, 30]. B_{c1} cannot be tracked to low enough angle to obtain a reliable fit for γ. With the field-angle phase diagram determined, we now investigate whether the XXZ-J_1-J_3 model can provide a good description of both its qualitative and quantitative features.

Monte Carlo simulations of the classical model

Using classical Monte Carlo methods, we compute the magnetotropic susceptibility for various field strengths and angles. We use an XXZ-J_1-J_3 model with small bond-dependent anisotropies presented by Halloran et $al.$ [14] with the addition of a Zeeman term coupling spins to the magnetic field. We write this Hamiltonian as $\mathcal{H} = \mathcal{H}_{\mathrm{XXZ}} + \mathcal{H}_{\mathrm{anisotropy}} + \mathcal{H}_{\mathrm{Zeeman}}$.
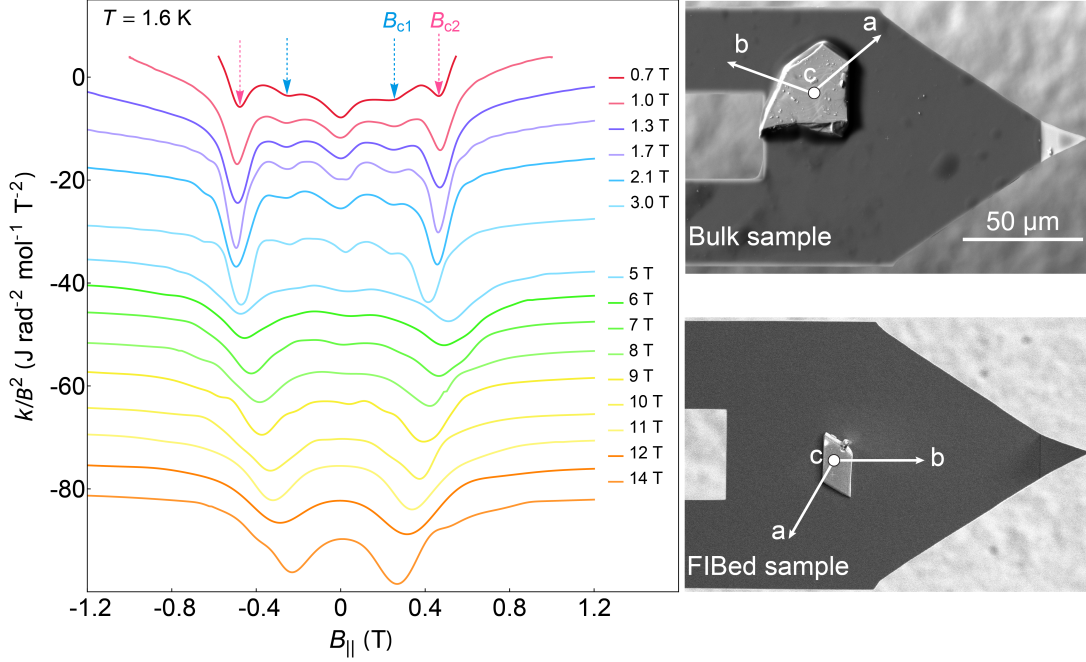
FIG. 3. **Critical fields of BaCo$_2$(AsO$_4$)$_2$ at $T = 1.6$ K.** The magnetotropic susceptibility normalized by B^2, plotted versus the in-plane magnetic field $B_{||} \equiv B \sin \theta$, and offset for clarity. The large change in k near B_{c2} for fields close to the c-axis limits our ability to track the resonant frequency at high fields. Therefore, to reduce the signal to a measurable range across all field angles, we measured a FIB'ed crystal with a volume ~ 50 times smaller than the bulk sample for $B \geq 5$ T. SEM images of the two measured samples are shown next to the corresponding data. The lower-field data (≤ 3 T) has been multiplied by 3.5 for clarity on this scale (see SI for details on unit conversions and scaling factors between cantilevers and crystals).

$$\mathcal{H}_{\text{XXZ}} = \sum_{n=1,3} \sum_{\langle i,j \rangle_n} \left(J_{xy}^{(n)} \left(S_i^x S_j^x + S_i^y S_j^y \right) + J_z^{(n)} S_i^z S_j^z \right)$$

$$\mathcal{H}_{\text{anisotropy}} = \sum_{\langle i,j \rangle \in \lambda} \left(D_\lambda \left(S_i^x S_j^x - S_i^y S_j^y \right) + E_\lambda \left(S_i^x S_j^y + S_i^y S_j^x \right) \right) \quad (2)$$

$$\mathcal{H}_{\text{Zeeman}} = -\mu_{\text{B}} B \sum_i \left(g_{ab} \sin(\theta) \left(S_i^x \cos(\phi) + S_i^y \sin(\phi) \right) + g_c \cos(\theta) S_i^z \right)$$

where $\lambda = \{x, y, z\}$ are labels for the three different first nearest-neighbour bond directions. The details of the bond-dependent couplings, D_λ and E_λ, are presented in the SI VI. The exchange parameters used in the current work are slightly different from those in Halloran *et al.* [14]. The refined parameter set is presented in the SI VI and provides a better agreement with the magnetization data. Because all observables are largely independent of the angle ϕ (measured away from the a-axis), both in experiments and in our simulations [14], we choose to explore $\phi = 0$ for simplicity. The calculations were performed at $T = 1.6$ K to match the experimental temperature.

We identify two minima in the magnetotropic susceptibility that correlate well with the transition to the 1/3 magnetization plateau and to the fully polarized state Figure 4A. This is qualitatively similar to the experimental data. We further confirm these phases to be the incommensurate spiral ($|\mathbf{q}_c| \approx 0.29$), the $|\mathbf{q}_c| = 1/3$ phase, and the polarized paramagnet by examining the peaks in the static spin structure factor.

By tracking the two minima in the calculated magnetotropic susceptibility as a function of angle, we produce the phase diagram shown in Figure 4B. The shapes of the resulting curves ($B_{c1}(\theta)$ and $B_{c2}(\theta)$) match extremely well with experiment. We also compute γ for B_{c2} and find $\gamma = 30$. This is in agreement with the experimentally determined value of 31 above. We note that while the qualitative features of the calculated phase diagram are in good agreement with those of the experimental phase diagram, the overall calculated field scale is larger by more than 50%.
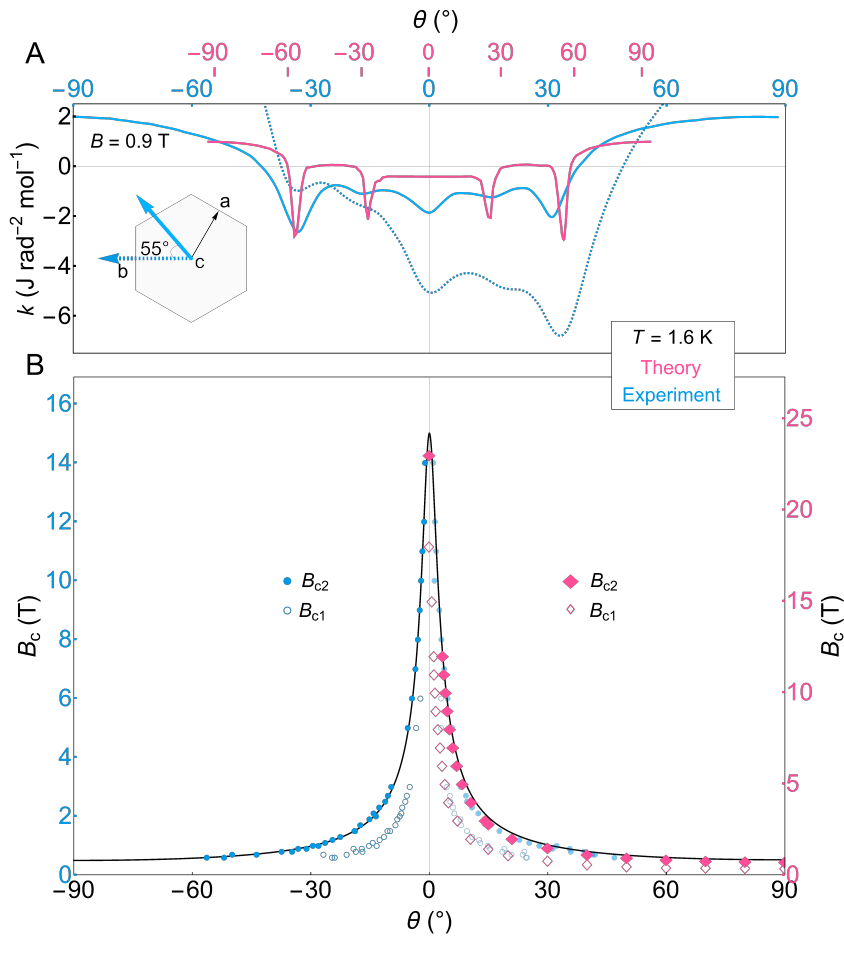
FIG. 4. **Comparison between experimental and theoretical results.** A) The magnetotropic susceptibility of $BaCo_2(AsO_4)_2$ at $T = 1.6$ K and $B = 0.9$ T for rotation of magnetic field in two different crystal planes: the dashed blue line corresponds to rotation from the c-axis ($\theta = 0°$) towards the b-axis ($\theta = 90°$), and the solid blue line shows rotation from the c-axis into the ab-plane at an angle $\sim 55°$ from the b-axis. The colored arrows on the honeycomb (inset) illustrate the two planes of rotation. The solid blue data has been scaled by 3.5. The angle in the Monte Carlo results has been scaled by 1/1.6, the same scaling factor needed to match the experimental and theoretical critical fields (Figure 11). B) The pink points show the transition fields from Monte Carlo results plotted versus field angle. The blue points show B_{c1} and B_{c2} selected from both angle sweep (Figure 3) and field sweep data (Figure 2). The black lines through the B_{c2} data points are fits of the experimental (theoretical) data to Equation 1 on the $-\theta$ ($+\theta$) side. The calculations of the critical fields qualitatively capture the angle dependence of both B_{c1} and B_{c2}, but the overall field scale is 1.6 times larger than observed.

iDMRG quantum phase diagram

To investigate the quantitative discrepancy in the values of the critical fields between the experiment and Monte-Carlo simulations, we use iDMRG [22–25] of the quantum model to study the nature of the ground state at zero field. We simulate the XXZ-J_1-J_3 model without the D_λ and E_λ anisotropies (SI VI). These small bond-dependent interactions are omitted to numerically leverage the continuous $U(1)$ symmetry of the $\mathcal{H}_{XXZ}$ Hamiltonian. A similar model was recently investigated with DMRG [8], variational Monte-Carlo [10], and pseudo-Fermion functional renormalization group [31]. Unlike DMRG on a finite slab, iDMRG on an infinite cylinder can capture incommensurate orders with a continuously varying ordering wavevector, which is of particular relevance for the ground state of $BaCo_2(AsO_4)_2$.

Varying the ratio of first $J_{xy}^{(1)}$ and third-nearest-neighbour in-plane coupling $J_{xy}^{(3)}$, we find magnetically ordered phases that can be identified by tracking the position of the magnetic Bragg peak in the static spin structure factor. In the quantum phase diagram shown in Figure 5A, we can clearly identify the ferromagnet ($|\mathbf{q}_c| = 0.0$), the zig-zag ($|\mathbf{q}_c| = 0.5$), and the incommensurate ordered phases with peaks at continuously varying points $|\mathbf{q}_c|$ along the $\Gamma - M$ direction (see inset). Compared with the classical phase boundaries in Figure 5B, the parameter regime where the incommensurate order is stabilized is greatly reduced in the quantum model. In particular, we find that the quantum
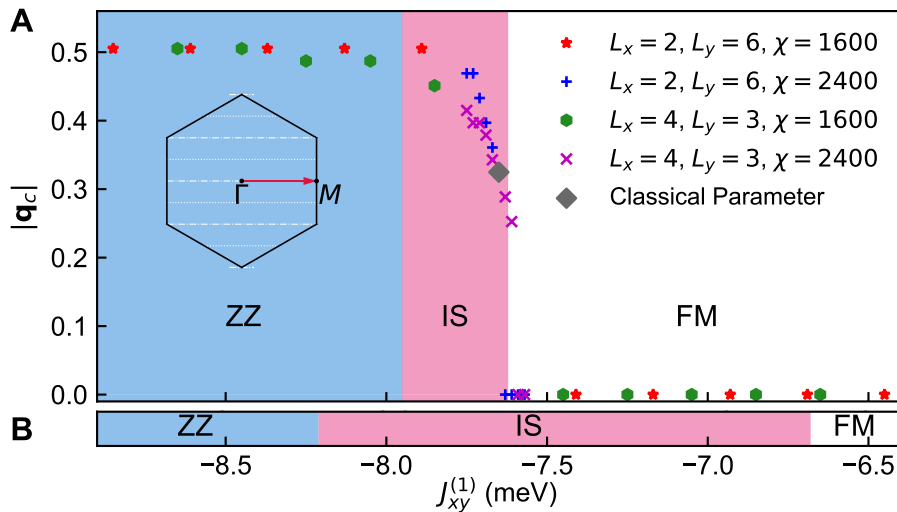
FIG. 5. **Quantum Phase diagram using iDMRG** (A) The position of the peak in the static spin structure factor $|\mathbf{q_c}|$ is used to identify the various phases: ferromagnet (FM, $|\mathbf{q}_c| = 0.0$), zig-zag (ZZ, $|\mathbf{q}_c| = 0.5$), and incommensurate state (IS) with $|\mathbf{q}_c|$ at wavevectors between $\Gamma - M$ (along red arrow in inset). An XC cylindrical geometry was used in iDMRG with an MPS unit cell size L_y along the circumference, L_x along the infinite direction, and a bond dimension χ. The BZ in the inset shows the momentum cuts along which the spin structure factor can be accessed in this cylindrical geometry, dotted lines for $L_y = 6$, and dashed-dotted lines for both $L_y = 3$ and $L_y = 6$. We have used $J_z^{(1)} = -1.2$ meV, $J_z^{(3)} = -0.8$ meV and the constraint $J_{xy}^{(1)} + J_{xy}^{(3)} = -5.0$ meV. At the best-fit classical parameter of $J_{xy}^{(1)} = -7.65$ meV, the ground state (grey diamond) is in the IS phase, but is close to the phase boundary between the FM and the IS. (B) The classical phase boundaries obtained using variational single Q-ansatz and simulated annealing for the same parameters as in (A). The region of stability of the IS in the quantum phase diagram is reduced compared to (B) due to quantum fluctuations.

ground state using the exchange couplings for $\mathcal{H}_{\mathrm{XXZ}}$ used in this work is incommensurate (SI VI), but in very close proximity to the phase boundary of the ferromagnetic state. In addition, if we use the set of exchange parameters (excluding small anisotropy terms) considered in a previous DMRG study [8], we obtain a ferromagnetic ground state. This is consistent with their result and our conclusion of the proximity to the ferromagnetic state. Note that the parameters in Jiang *et al.* [8] are slightly different from the original parameters in Halloran *et al.* [14], as well as the refined set used in the current work. Detailed comparison between these results is discussed in the SI V. The clear reduction of the incommensurate state's stability suggests that quantum fluctuations of the ferromagnetic state may suppress the critical fields of the nearby incommensurate state.

Discussion

The classical simulations reproduce several features of the experimental phase diagram. For example, the calculated ratio of B_{c2} to B_{c1} is ~ 1.9, which agrees well with the experimentally-determined value of ~ 1.9 (SI III). The classical simulations find that the anisotropy in B_{c2} is $\gamma = 30$, again very close to the experimental value of $\gamma = 31$. Even the structure of the simulated magnetotropic susceptibility data is qualitatively consistent with the measured data, revealing two distinct peaks that correspond to phase transitions from the incommensurate phase to the $|\mathbf{q}_c| = 1/3$ phase and then from the $|\mathbf{q}_c| = 1/3$ phase to the polarized paramagnet. Further, the change in the magnitude of the calculated magnetotropic susceptibility at B_{c1} and B_{c2} is within a factor of two of the measured values (Figure 4).

The most obvious discrepancy between the data and the Monte Carlo simulations of the classical model is that the simulations overestimate the critical fields by roughly a factor of 1.6. The iDMRG results shed light on this issue. We find that iDMRG simulations using roughly the same best-fit exchange parameters obtained from the classical simulations find an incommensurate ordered state that is very close to the phase boundary with the nearby ferromagnetic state (see Figure 5). The enhanced stability of the ferromagnetic state in the quantum model explains the decrease in the critical fields in the experiment as likely due to quantum zero-point fluctuations in the ordered phases.

The level of qualitative agreement between experiments and Monte Carlo simulations of the classical model indicates that, even though quantum fluctuations are important in determining the quantitative position of the phase boundaries and corresponding ground states, most of the physics can be understood in terms of classical dynamics of long-range ordered states. Our measurement and analysis further suggest that the incommensurate state remains the ground

state for an out-of-plane field up to more than $B = 10$ T. This observation is at odds with Ref. [17], where a field-induced QSL was proposed to be stabilized for a magnetic field beyond $B = 4.5$ T. These considerations thus cast doubt on previous claims of the realization of QSL physics in $BaCo_2(AsO_4)_2$ for the explored parameter regime. Our detailed phase diagram (Figure 4) is highly suggestive of the following interpretation: due to the gigantic easy-plane anisotropy of $BaCo_2(AsO_4)_2$, the slight misalignment of the crystal with respect to magnetic field identified by Zhang *et al.* [17] causes the system to enter the intermediate $|\mathbf{q}_c| = 1/3$ phase, rather than the field-polarized phase, for a field of approximately $B = 4$ T. Thus, the observed change in the terahertz spectrum at $B = 4$ T could correspond to a change in the magnon gap as the system transitions from the incommensurate to the intermediate phase at B_{c1}, rather than the appearance of a QSL at B_{c2}. This interpretation is supported by preliminary inelastic neutron scattering experiments [32].

While many aspects of the $BaCo_2(AsO_4)_2$ phase diagram are captured by the XXZ-J_1-J_3 model, the importance of other symmetry-allowed anisotropic spin interactions remains an open question. For example, one feature of the data that is not captured in the classical simulations is the asymmetry in the magnitude of k when rotating from $\theta \to -\theta$ (Figure 4A). This asymmetry is not present in our MC calculations due to an underlying symmetry of the model Hamiltonian. Specifically, note that taking $\theta \to -\theta$ is equivalent to taking $B_x \to -B_x$ and $B_y \to -B_y$ while leaving B_z unchanged. The interacting part of our model Hamiltonian also has such an in-plane inversion symmetry under $(S_x, S_y) \to (-S_x, -S_y)$. When taking $\theta \to -\theta$, S_x can be re-labeled as $-S_x$ and likewise for S_y, leaving the partition function (and therefore the free energy and the magnetotropic susceptibility) unchanged. The asymmetric measurements of k reveal the need for additional terms in the model Hamiltonian which couple the in-plane spin components (S_x and S_y) to S_z.

While we expect all of the anisotropic interactions to be much smaller than the main XXZ exchange parameters, the determination of these small interactions would provide the accurate estimation of the sub-leading bond-dependent interactions such as the Kitaev and Γ interactions in the local spin coordinate. This would help us understand potential avenues to enhance such bond-dependent interactions.

Methods

I. Crystal synthesis

Polycrystalline samples of $BaCo_2(AsO_4)_2$ were produced by the heating of well-ground mixtures of $BaCO_3$ (Strem Chemicals, 99.9%), Co_3O_4 (NOAH Technologies, 99.5%, 325 mesh), and $NH_4H_2AsO_4$ (Alfa Aesar, 98%) in a 2.9 : 2 : 6 molar ratio. The mixture was placed in an uncovered alumina crucible in air, heated to 305°C, held for 12 hours, heated to 875°C, held for 48 hours, cooled to room temperature, and finally heated to 925°C for 12 hours before again cooling to room temperature. All ramp rates were set at 100°C per hour.

While $BaCo_2(AsO_4)_2$ melts incongruently under most atmospheric conditions, we found that single crystals could be grown via a modified Bridgeman technique. Polycrystalline samples were packed into a cylindrical alumina crucible with a pointed tip, which was then sealed under vacuum in a 12mm ID, 16mm OD quartz tube. The tube was then suspended in a vertical tube furnace, just above a hollowed block of firebrick. The sample was heated to 1175°C at a rate of 100°C per hour and held for 12 hours without translation to ensure a homogeneous melt. The tube was then translated downward through the firebrick at a nominal rate of 3.0 mm per hour until the entire crucible had passed into the cooler zone. Furnace heating was then turned off and the sample was allowed to cool naturally within the firebrick. The static vacuum atmosphere was found to be necessary to achieve congruent melting in this system. The resulting mass of crystals was then pried from the crucible and mechanically separated along the cleavage planes.

II. Vibrating sample magnetometry (VSM) data

II.1. Nearly in-plane magnetization

Using vibrating sample magnetometry (VSM), we measured the magnetization of $BaCo_2(AsO_4)_2$ at several temperatures with the magnetic field applied at 75° from the c-axis (Figure 7) in order to compare with magnetotropic measurements performed at the same field angle. A single crystal of $BaCo_2(AsO_4)_2$ with an approximate volume of 0.41 mm^3 (Figure 6A) contains approximately 4.8×10^{18} cobalt atoms. We used the VSM option of a Quantum Design Dynacool Physical Property Measurement System (PPMS) with a 14 T magnet. The measured magnetization is read in emu units ($1 = 1.08 \times 10^{20}$ μ_B), which was divided by the estimated number of cobalt above to obtain the magnitude displayed in Figure 7A.

We find that the magnetization as a function of a nearly in-plane magnetic field is consistent with previous studies done with magnetic field applied *in* the honeycomb plane. As the lowest temperatures of $T = 1.8$ K, the magnetization saturates at $B = 0.5$ T with a magnetic moment of $\sim$2.5 μ_B per cobalt (Figure 7A). At low temperatures, there is also a clear transition into the $M = 1/3$ plateau in the field range from roughly 0.2 to 0.5 T. As temperature increases, the saturation field also increases. The field-derivatives of the magnetization curves in panel A are shown in panel B of Figure 7. The positions of B_{c1} and B_{c2} used to construct the phase diagram in (Figure 1B) are indicated with black and red points, respectively.

II.2. Out of plane magnetization of $BaCo_2(AsO_4)_2$

We measured the magnetization of $BaCo_2(AsO_4)_2$ for magnetic field applied along the c-axis. Using the Photonic Science Laue X-ray Detector, we identified the c-axis of the sample and aligned it with the external magnetic field with $<0.15°$ of uncertainty. The c-axis magnetization measurements were performed on the sample in Figure 8, which has a volume of 0.87 mm^3 that consists of approximately 1×10^{19} cobalt atoms. The measured c-axis magnetization in units of μ_B per cobalt is shown in Figure 9.

III. Magnetotropic measurements

III.1. Unit conversion

In resonant torsion magnetometry, we infer the anisotropic magnetic response of the sample by measuring a shift in the resonant frequency of a cantilever as external parameters (temperature, magnetic field, field angle) are changed. In order to have an intuitive understanding of the magnitude of the frequency shift (proportional to the magnetotropic
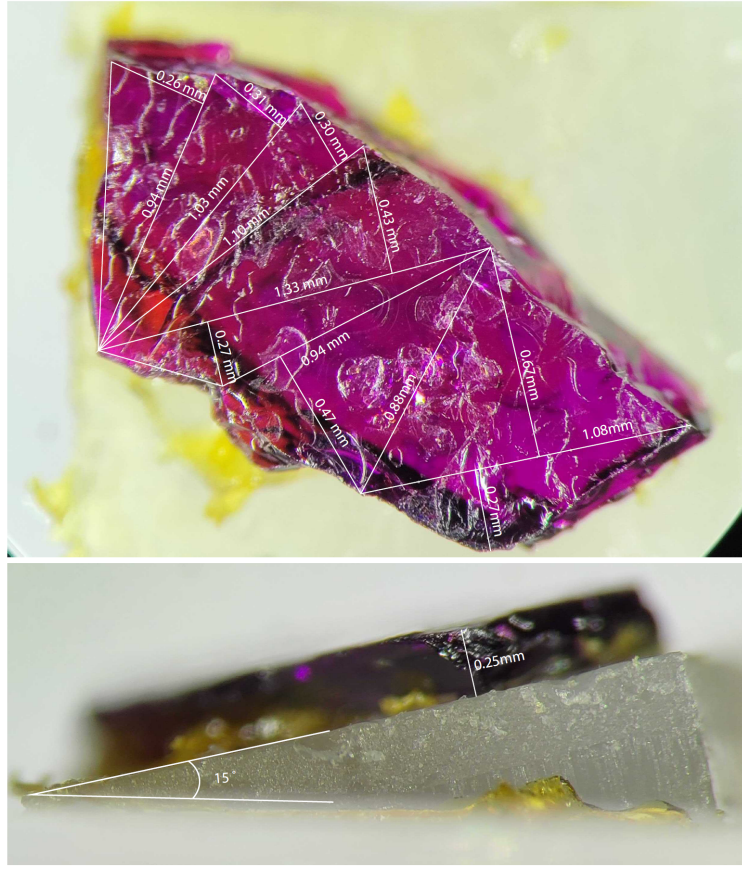
FIG. 6.   A) Single crystal of $BaCo_2(AsO_4)_2$ B) Side view of the crystal in panel A mounted on a teflon wedge with a $15°$ angle using GE varnish. VSM measurements were performed on this sample with magnetic field applied at an angle $15°$ from the honeycomb plane towards the c-axis.
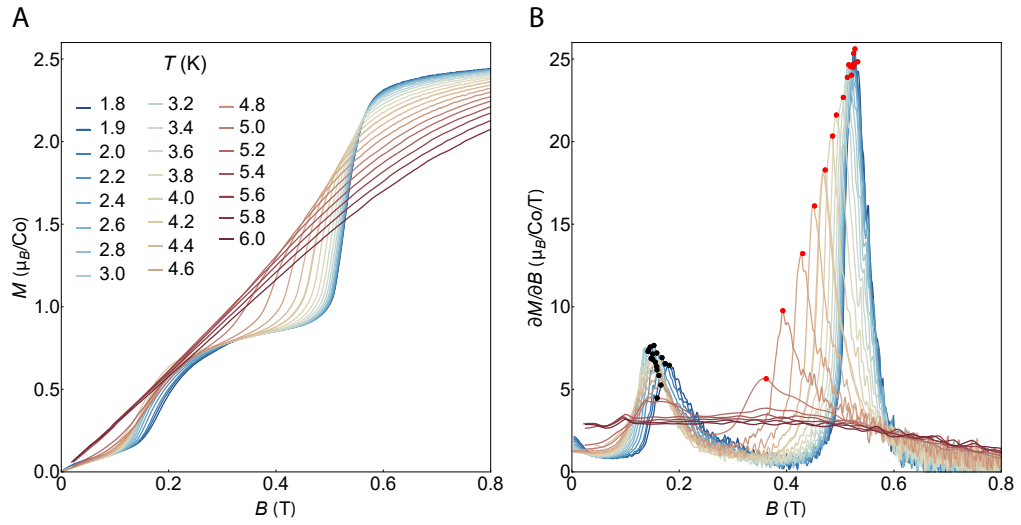

FIG. 7.   A) Temperature-dependent magnetization of $BaCo_2(AsO_4)_2$ for field applied nearly in-plane ($\theta = 75°$). B) The field-derivatives of the magnetization shown in panel A used to identify the positions of the critical fields, B_{c1} and B_{c2}.
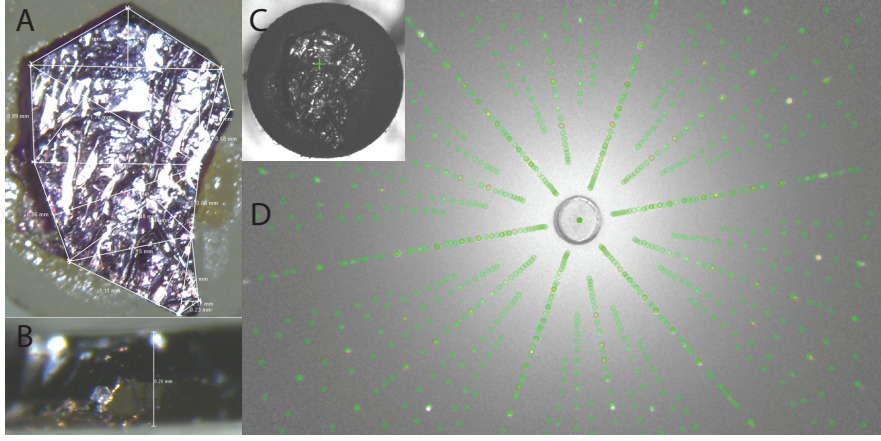
FIG. 8. A) Large single crystal of $BaCo_2(AsO_4)_2$ used for c-axis VSM measurements. B) The side view of the crystal in panel A mounted on a cylinder. The thickness of the crystal is. C) Optical image of the top of the sample mounted on a cylinder for Laue diffraction. D) The white points show the measured intensity of the diffraction pattern of $BaCo_2(AsO_4)_2$ overlaid with the simulated c-axis spectra in green.
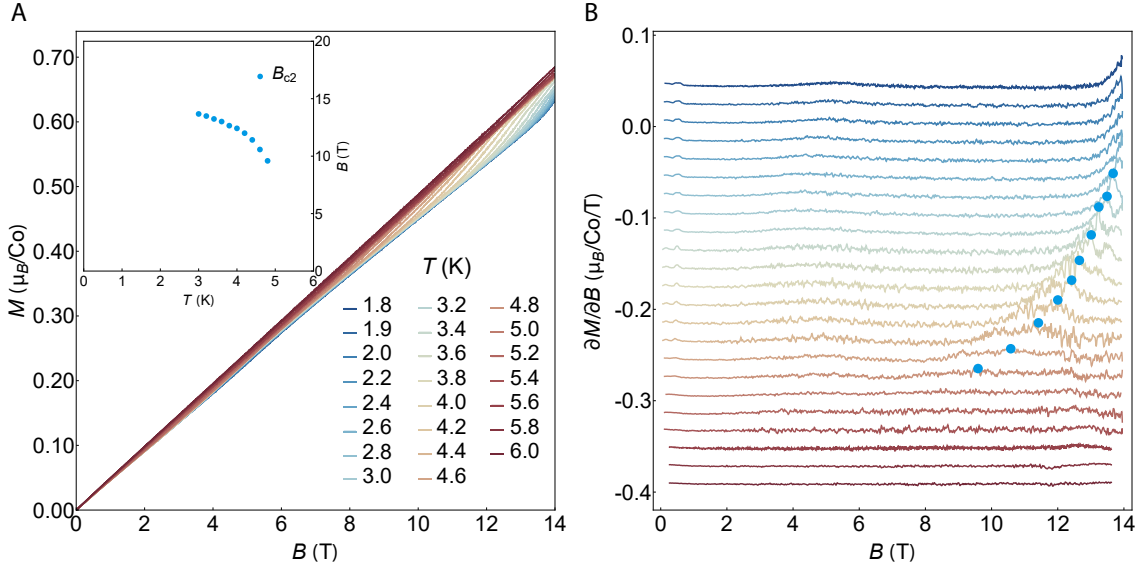

FIG. 9. A) Temperature-dependent magnetization of $BaCo_2(AsO_4)_2$ for field applied perpendicular to the honeycomb planes ($\theta = 0°$). The inset shows critical field B_{c2} as a function of temperature. B) The field-derivatives of the magnetization shown in panel A used to identify the positions of the critical field, B_{c2}.

susceptibility, k), we calibrate the measured response in the linear regime by using the known anisotropic magnetic susceptibility χ_{ii} and χ_{jj} at $T = 100$ K.

To convert the frequency shift into energy units, we first find the molar concentration of cobalt atoms in the measured sample by estimating the sample volume based on SEM images. The estimated volume of the FIB'ed sample shown in Figure 3 is 161 μm^3 and the unit cell size is 510 $Å^3$, corresponding to 3.2×10^{11} unit cells. Each unit cell contains 6 cobalt, leading to roughly 3.14 pmol of Co in the smaller FIB'ed sample. Estimates similarly obtained for the larger bulk crystal (upper SEM image in Figure 3) give 98.4 pmol of Co.

Taking into account the relations $k = \partial\tau/\partial\theta$, $\tau = M \times B$, and $M = \chi H$, the magnetotropic susceptibility in the linear regime is:

$$k = (\chi_c - \chi_a)\mu_0 H^2 \cos 2\theta, \tag{3}$$

where χ_a and χ_c represent the $a-$ and $c-$axis magnetic susceptibility, respectively.

Given the magnetic susceptibility values obtained from Zhong *et al.* [1], we can calculate the magnetotropic suscepti-bility in units of joules per mole. Figure 10 shows k as a function of angle at $\mu_0 H = 1$ T and $T = 100$ K as calculated using the known magnetic susceptibility (orange curve). The blue curve shows the raw frequency shift per mole at the same field and temperature. The ratio of the orange curve to the blue curve provides the scaling factor that is then applied to all data sets.

The FIB'ed sample (containing 3.14 pmol of cobalt atoms) shown in Figure 3 produces a frequency shift of ~ 0.055 Hz at $B = 1$ T and $T = 100$ K. The ratio of the maximum values for each curve provide a scaling factor to convert the frequency shift to joule unit. This scaling factor is 15.5 pJ per rad^2 per Hz.
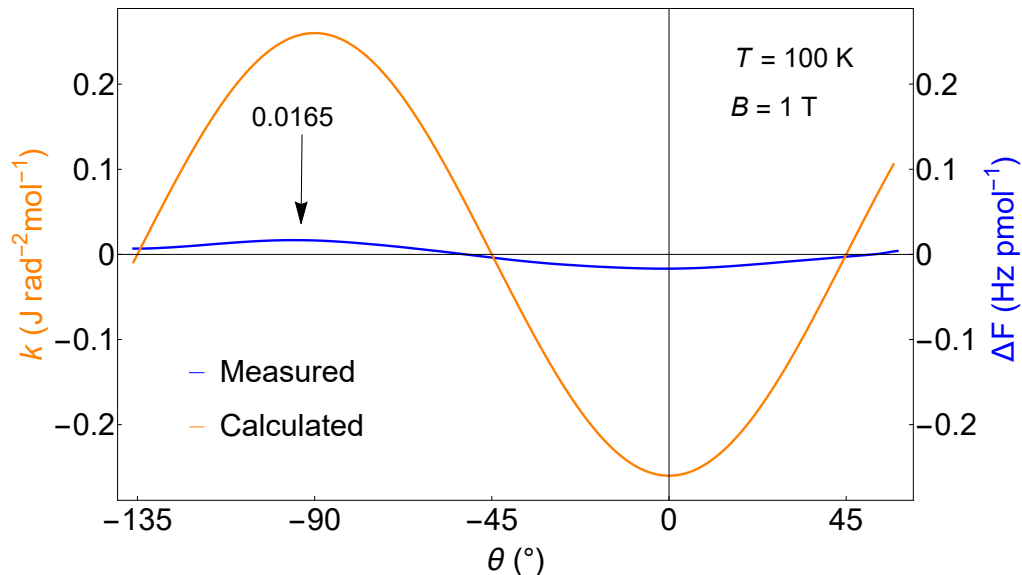

FIG. 10. The magnetotropic susceptibility calculated from the known anisotropic magnetic susceptibility in the *ac*-plane [1]. The blue curve shows the measured frequency shift at the same field and temperature as the calculated orange curve. The ratio in the amplitudes of the cosθ curves provides a scaling factor to convert the measured frequencies into energy units. We find that 1 Hz = 15.5 pJ.

IV. Monte Carlo calculations

Our Monte Carlo (MC) calculations were performed using the Metropolis algorithm, employing parallel tempering and overrelaxation sweeps allowing them to converge more rapidly. The metropolis algorithm updates spins by first proposing a random change to a spin and then accepting that change with a probability min$(e^{-\beta \Delta E}, 1)$. We perform this procedure for every spin in the simulation, thus performing a full Metropolis sweep. In addition to this type of update, we also use overrelaxation sweeps. These involve flipping a spin across the local effective field at each site

$$\mathbf{S}_i \rightarrow -\mathbf{S}_i + 2 \frac{2\mathbf{S}_i \cdot \mathbf{B}_i^{\text{eff}}}{|\mathbf{B}_i^{\text{eff}}|^2} \mathbf{B}_i^{\text{eff}}. \tag{4}$$

These sweeps do not change the energy of the spin configuration and so allow us to more rapidly explore the space of all possible spin configurations. We perform 10 of these overrelaxation sweeps for every Metropolis sweep. Fur-thermore, we use parallel tempering wherein many different temperatures are simulated simultaneously and their spin configurations are swapped with one another with probability min$(e^{\Delta \beta \Delta E}, 1)$. We propose such a swap between adjacent temperature simulations every 20 MC sweeps. Monte Carlo calculations were performed using a $24 \times 24 \times 2$ system size. After waiting 5×10^6 MC sweeps for the system to thermalize, 10^5 measurements were taken, waiting 100 sweeps between each measurement to avoid auto-correlation. For values of B and θ near the phase boundaries, the results of up to 50 separate simulations were averaged together to improve accuracy. For other points, only a single Markov chain was needed. Magnetotropic susceptibility was computed from the measured spin configurations
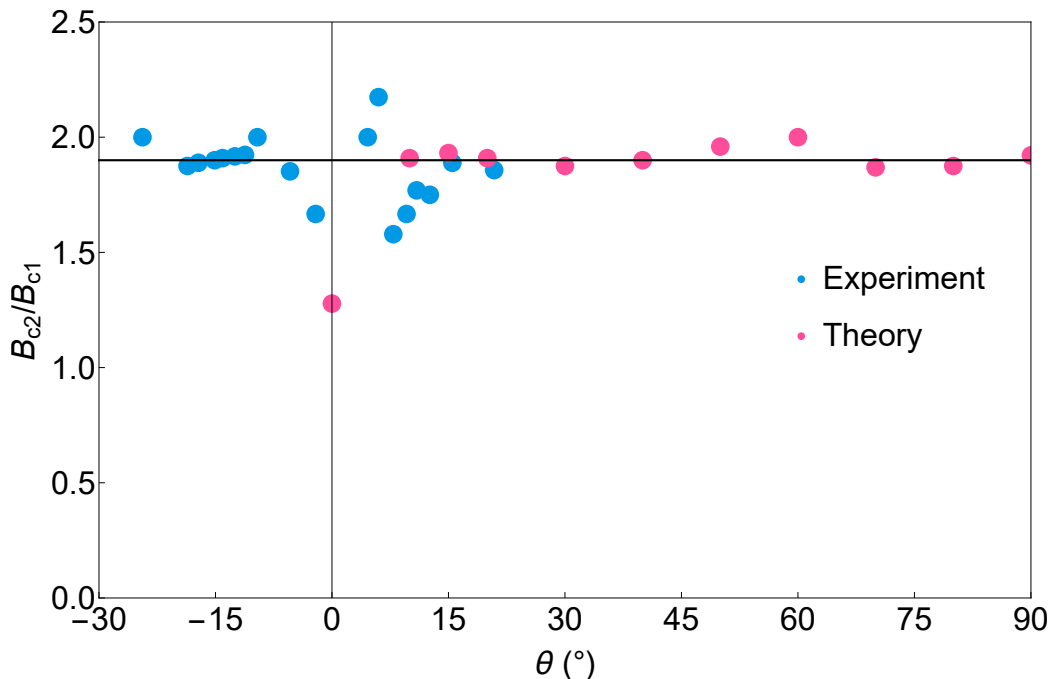
FIG. 11. The experimental and calculated ratio of B_{c2} to B_{c1}. The solid horizontal line is a guide to the eye at $B_{c2}/B_{c1} = 1.9$. The calculated ratio drops near $\theta = 0°$: B_{c1} is not visible in the experimental data at this angle.

using Equation 5.

$$k = (\mathbf{n} \times \mathbf{B}) \cdot (\mathbf{n} \times \mathbf{M}) - (\mathbf{n} \times \mathbf{B})^T \chi (\mathbf{n} \times \mathbf{B}) \tag{5}$$

where $\mathbf{n}$ is the axis about which the rotation occurs. For the MC calculations performed here, $\mathbf{B}$ was kept strictly in the ac-plane and therefore $\mathbf{n}$ is a unit vector perpendicular to this plane. This is the definition of magnetotropic susceptibility comes from [21].

V. iDMRG calculations

iDMRG was implemented using the python package TeNPy [26]. In iDMRG a 1D Matrix Product State (MPS) representation of the wavefunction is used to represent the 2D system by snaking around the MPS unit cell. iDMRG variationally optimizes this MPS wavefunction into the ground state. For our simulations, an XC cylindrical geometry was used. The MPS unit cell had a circumference length L_y and length L_x in the infinite direction. As iDMRG gives us access to long-range correlations in the infinite direction, the XC geometry permits the computation of a high-density cut of the spin structure factor between the Γ and M point in the Brillouin zone (see Figure 5 (a) inset).

The Hamiltonian H_{XXZ} has a $U(1)$ symmetry of rotations in the x-y plane, and this symmetry is encoded into its MPS representation. Correspondingly, $S^z_{tot} = \sum_i S^z_i$ is conserved as $[S^z_{\text{tot}}, H] = 0$. In this study, we have focused only on the $S^z_{tot} = 0$ sector of the spin model.

For the iDMRG, we have followed a two-step routine. We start from an up/down product state and run a maximum of 40 sweeps with the density matrix mixer turned on to escape from any local minima in the energy landscape. Then we run a maximum of 100 sweeps or until $\Delta E = 10^{-8}$ with the density matrix mixer turned off to converge into the ground state in the global minima basin.

As shown in Figure 5, we have performed our iDMRG simulations for different MPS unit cell sizes (L_x, L_y), and different bond dimensions χ. Even though the phase boundaries weakly depend on these choices due to finite size effects from wrapping around a cylinder and the truncation of less relevant entanglement information, the overall structure of the phase diagram is unaffected.

For a consistency check with the finite slab DMRG simulations in [8], we used the same parameter set for the XXZ-J_1-J_3 model without the bond-dependent anisotropies in an iDMRG simulation. The parameter set from [8]
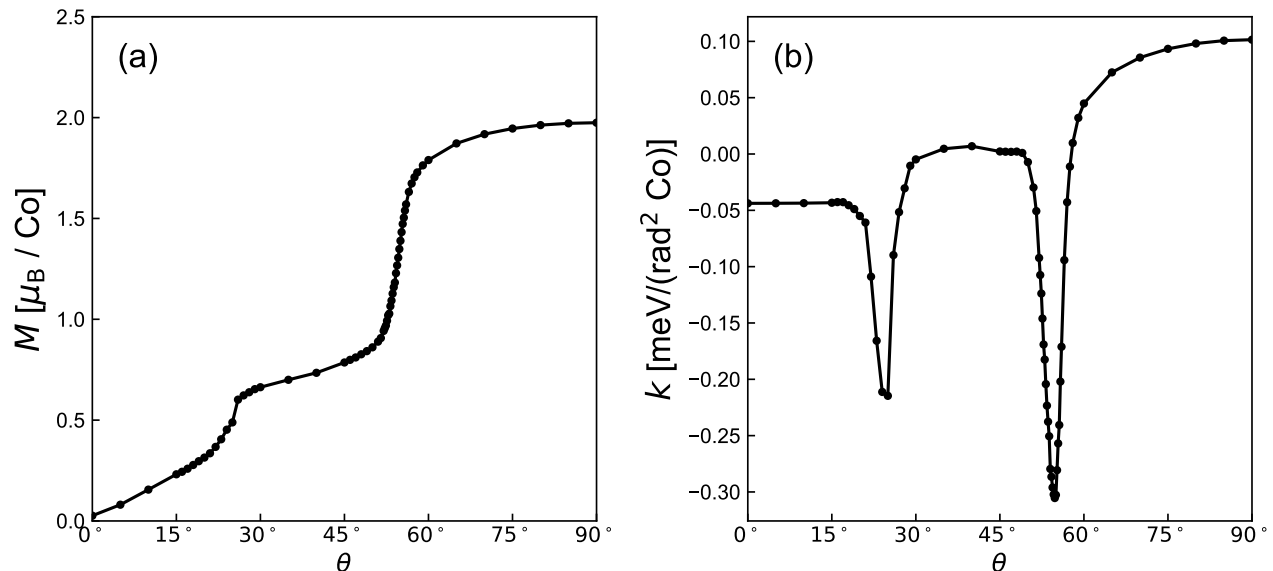
FIG. 12. Results from Monte Carlo calculations shown at fixed temperature ($T = 1.5$ K) and magnetic field strength ($B = 0.9$ T) as a function of applied field angle θ. (a) Shows magnetization per site, with the characteristic $M = 1/3$ plateau corresponding to the commensurate $q = 1/3$ phase. (b) Shows magnetotropic susceptibility per site as a function of θ. The two peaks in k coincide with the steep increase in magnetization thus we use these peaks to identify the phase boundaries.

corresponds to $J_{xy}^{(1)} = -1.00$, $J_{xy}^{(1)}/J_{xy}^{(3)} = -3.00$, $J_z^{(1)}/J_{xy}^{(1)} = 0.13$ and $J_z^{(3)}/J_{xy}^{(3)} = -0.35$. Even without the bond-dependent anisotropies, we find a ferromagnetic ground state, this is in agreement with the results of [8]. However, the ratios $J_z^{(1)}/J_{xy}^{(1)}$ and $J_z^{(3)}/J_{xy}^{(3)}$ used in the parameter set from [8] do not match with Eq 13 of Ref. [14] or our more refined parameter set in Equation 7.

VI.   Model Parameters in Monte Carlo and iDMRG simulations

The parameters D_λ and E_λ in Eq. 2 are explicitly

$$D_\lambda = D \cos(2\alpha_\lambda) - E \sin(2\alpha_\lambda)$$
$$E_\lambda = D \sin(2\alpha_\lambda) + E \cos(2\alpha_\lambda)$$

(6)

where $\alpha_\lambda = +2\pi/3, -2\pi/3, 0$ for $\lambda = x, y, z$ respectively. The values of parameters used for all MC calculations are

$$
\begin{array}{ll}
J_{xy}^{(1)} = -7.65\text{meV} & J_{xy}^{(3)} = +2.64\text{meV} \\
J_z^{(1)} = -1.20\text{meV} & J_z^{(3)} = -0.81\text{meV} \\
D = +0.10\text{meV} & E = -0.10\text{meV} \\
g_{ab} = 5.0 & g_c = 2.7
\end{array}
$$

(7)

these are a refined version of the parameter set in [14], modified slightly to improve agreement with experimentally observed critical fields. For the iDMRG simulations shown in Figure 5 (a), we have used $J_z^{(1)} = -1.20$ meV and $J_z^{(3)} = -0.80$ meV. Further, we have used the constraint $J_{xy}^{(1)} + J_{xy}^{(3)} = -5.00$ meV to compare with the classical phase diagram presented in Figure 6 e in Ref. [14].

----

* kimberly.modic@ist.ac.at

[1] R. Zhong, T. Gao, N. P. Ong, and R. J. Cava, Weak-field induced nonmagnetic state in a Co-based honeycomb, Science Advances **6**, eaay6953 (2020), 1910.08577.

[2] A. Kitaev, Anyons in an exactly solved model and beyond, Annals of Physics 10.1016/j.aop.2005.10.005 (2006), cond-mat/0506438.

[3] H. Takagi, T. Takayama, G. Jackeli, G. Khaliullin, and S. E. Nagler, Concept and realization of Kitaev quantum spin liquids, Nature Reviews Physics **1**, 264 (2019), 1903.08081.

[4] H. Liu and G. Khaliullin, Pseudospin exchange interactions in d7 cobalt compounds: Possible realization of the Kitaev model, Physical Review B **97**, 014407 (2018), 1710.10193.

[5] R. Sano, Y. Kato, and Y. Motome, Kitaev-Heisenberg Hamiltonian for high-spin d7 Mott insulators, Physical Review B **97**, 014408 (2018), 1710.11357.

[6] H. Liu, J. Chaloupka, and G. Khaliullin, Kitaev Spin Liquid in 3d Transition Metal Compounds, Physical Review Letters **125**, 047201 (2020), 2002.05441.

[7] X. Liu and H.-Y. Kee, Non-Kitaev versus Kitaev honeycomb cobaltates, Physical Review B **107**, 054420 (2023), 2211.03737.

[8] S. Jiang, S. R. White, and A. L. Chernyshev, Quantum phases in the honeycomb-lattice J1–J3 ferro-antiferromagnetic model, Physical Review B **108**, L180406 (2023), 2304.06062.

[9] P. A. Maksimov, Proximity-induced sequence of field transitions in the Kitaev candidate BaCo2(AsO4)2, Physical Review B **108**, L180405 (2023), 2308.10672.

[10] A. Bose, M. Routh, S. Voleti, S. K. Saha, M. Kumar, T. Saha-Dasgupta, and A. Paramekanti, Proximate Dirac spin liquid in honeycomb lattice J_1-J_3 XXZ model: Numerical study and application to cobaltates, arXiv 10.48550/arxiv.2212.13271 (2022), 2212.13271.

[11] S. Das, S. Voleti, T. Saha-Dasgupta, and A. Paramekanti, XY magnetism, Kitaev exchange, and long-range frustration in the Jeff=12 honeycomb cobaltates, Physical Review B **104**, 134425 (2021), 2106.11982.

[12] P. A. Maksimov, A. V. Ushakov, Z. V. Pchelkina, Y. Li, S. M. Winter, and S. V. Streltsov, Ab initio guided minimal model for the "Kitaev" material BaCo2(AsO4)2: Importance of direct hopping, third-neighbor exchange, and quantum fluctuations, Physical Review B **106**, 165131 (2022), 2204.09695.

[13] S. M. Winter, Magnetic couplings in edge-sharing high-spin d 7 compounds, Journal of Physics: Materials **5**, 045003 (2022), 2204.09856.

[14] T. Halloran, F. Desrochers, E. Z. Zhang, T. Chen, L. E. Chern, Z. Xu, B. Winn, M. K. Graves-Brook, M. B. Stone, A. I. Kolesnikov, Y. Qui, R. Zhong, R. Cava, Y. B. Kim, and C. Broholm, Geometrical frustration versus Kitaev interactions in BaCo$_2$(AsO$_4$)$_2$, Proceedings of the National Academy of Sciences **120**, e2215509119 (2022), 2205.15262.

[15] Regnault and Rossat-Mignod, LP and, Effect of a magnetic field on the magnetic ordering of BaCo2 (AsO4) 2, Journal of Magnetism and Magnetic Materials **14**, 194 (1979).

[16] L.-P. Regnault, C. Boullier, and J. Lorenzo, Polarized-neutron investigation of magnetic ordering and spin dynamics in BaCo2(AsO4)2 frustrated honeycomb-lattice magnet, Heliyon **4**, e00507 (2018), 1801.06588.

[17] X. Zhang, Y. Xu, T. Halloran, R. Zhong, C. Broholm, R. J. Cava, N. Drichko, and N. P. Armitage, A magnetic continuum in the cobalt-based honeycomb magnet BaCo2(AsO4)2, Nature Materials **22**, 58 (2023), 2106.13418.

[18] Regnault and Rossat-Mignod, L. P. and, Phase Transitions in Quasi Two-Dimensional Planar Magnets, Springer, Dordrecht (1990).

[19] P. A. Maksimov and A. L. Chernyshev, Easy-plane anisotropic-exchange magnets on a honeycomb lattice: quantum effects and dealing with them, arXiv 10.48550/arxiv.2208.07617 (2022), 2208.07617.

[20] K. A. Modic, M. D. Bachmann, B. J. Ramshaw, F. Arnold, K. R. Shirer, A. Estry, J. B. Betts, N. J. Ghimire, E. D. Bauer, M. Schmidt, M. Baenitz, E. Svanidze, R. D. McDonald, A. Shekhter, and P. J. Moll, Resonant torsion magnetometry in anisotropic quantum materials, Nature Communications 2018 9:1 **9**, 1 (2018), 1802.08211.

[21] A. Shekhter, R. D. McDonald, B. J. Ramshaw, and K. A. Modic, Magnetotropic susceptibility, Physical Review B **108**, 035111 (2023), 2208.10038.

[22] S. R. White, Density matrix formulation for quantum renormalization groups, Physical Review Letters **69**, 2863 (1992).

[23] S. R. White, Density-matrix algorithms for quantum renormalization groups, Physical Review B **48**, 10345 (1993).

[24] U. Schollwöck, The density-matrix renormalization group, Reviews of Modern Physics **77**, 259 (2005), cond-mat/0409292.

[25] I. P. McCulloch, Infinite size density matrix renormalization group, revisited, arXiv 10.48550/arxiv.0804.2509 (2008), 0804.2509.

[26] J. Hauschild and F. Pollmann, Efficient numerical simulations with Tensor Networks: Tensor Network Python (TeNPy), SciPost Physics Lecture Notes , 005 (2018), 1805.00055.

[27] A. M. Ferrenti, M. A. Siegler, S. Ghosh, X. Zhang, N. Kintop, H. K. Vivanco, C. Lygouras, T. Halloran, S. Klemenz, C. Broholm, N. Drichko, and T. M. McQueen, Chemical tuning of a honeycomb magnet through a critical point, Physical Review B **108**, 064433 (2023).

[28] L. Y. Shi, X. M. Wang, R. D. Zhong, Z. X. Wang, T. C. Hu, S. J. Zhang, Q. M. Liu, T. Dong, F. Wang, and N. L. Wang, Magnetic excitations of the field-induced states in BaCo2(AsO4)2 probed by time-domain terahertz spectroscopy, Physical Review B **104**, 144408 (2021), 2106.13100.

[29] K. A. Modic, R. D. McDonald, J. P. Ruff, M. D. Bachmann, Y. Lai, J. C. Palmstrom, D. Graf, M. K. Chan, F. F. Balakirev, J. B. Betts, G. S. Boebinger, M. Schmidt, M. J. Lawler, D. A. Sokolov, P. J. Moll, B. J. Ramshaw, and A. Shekhter, Scale-invariant magnetic anisotropy in RuCl3 at high magnetic fields, Nature Physics 2020 17:2 **17**, 240 (2020), 2005.04228.

[30] X.-G. Zhou, H. Li, Y. H. Matsuda, A. Matsuo, W. Li, N. Kurita, G. Su, K. Kindo, and H. Tanaka, Possible intermediate quantum spin liquid phase in RuCl3 under high magnetic fields up to 100 T, Nature Communications **14**, 5613 (2023), 2201.04597.

[31] Y. Watanabe, S. Trebst, and C. Hickey, Frustrated Ferromagnetism of Honeycomb Cobaltates: Incommensurate Spirals, Quantum Disordered Phases, and Out-of-Plane Ising Order, arXiv 10.48550/arxiv.2212.14053 (2022), 2212.14053.

[32] T. Halloran, *GEOMETRICAL AND KITAEV FRUSTRATION IN SPIN-ORBIT COUPLED MAGNETS*, Ph.D. thesis (2023).